Baffled tubes with superimposed oscillatory flow: experimental study of the fluid mixing and heat transfer at low net Reynolds numbers

J. Muñoz-Cámara[a], D. Crespí-Llorens[b], J.P. Solano[a], P. Vicente[b]

[a] *Dep. Ing. Térmica y de Fluidos. Universidad Politécnica de Cartagena. Campus Muralla del Mar (30202). Cartagena (Spain).*
[b] *Dep. Ing. Mecánica y Energía. Universidad Miguel Hernández de Elche. Av. de la Universidad s/n (03202). Elche (Spain).*

Abstract

Experimental results of flow pattern and heat transfer in circular-orifice baffled tubes under pure oscillatory flow and compound flow conditions are presented. Hydrogen bubble visualization technique is employed for describing the unsteady flow structure, and particle image velocimetry is used in order to measure the velocity field during eight different phases of the oscillation cycle. The existence of a central jet and the cyclic dispersion of vortices upstream and downstream of the baffles is analyzed. The loss of the flow axisymmetry for $Re_{osc} > 130$ is clearly identified. Heat transfer measurements under uniform heat flux (UHF) conditions are obtained in a thermal-hydraulic rig, allowing for the description of the influence of net and oscillatory Reynolds numbers on the Nusselt number, using propylene-glycol as working fluid ($Pr = 150$). The impact of chaotic mixing, for $Re_{osc} > 150$, results in a uniform local heat transfer distribution along the reactor cell, as well as in thermal uniformity in the transverse plane of the tube.

Keywords: Oscillatory baffled reactors, Flow mixing, Oscillatory flow, PIV, Heat transfer enhancement

Nomenclature

$\dot{V}$ Volumetric flow rate

q'' Heat flux, W/m^2

Q Heat, W

x_0 oscillation amplitude, center to peak (m)

t time (s)

T temperature (°C)

A_h heat transfer area (m^2), $\pi D L_h$

c_p specific heat (J/(kg·K))

d orifice diameter (m)

D tube inner diameter (m)

f oscillation frequency (Hz)

k thermal conductivity (W/(m·K))

l cell length (m)

L_h heated length (m)

L_e length between the inlet temperature probe and the heated section beginning (m)

L_e length between the heated section end and the outlet temperature probe (m)

$n_s$number of interrogation windows

$R_v$axial-radial velocity ratio (-)

S open area (-), $(n \cdot d/D)^2$

U instantaneous mean flow velocity (m/s), based on D

U_n mean velocity of the net flow (m/s), based on D

x axial distance from the start of the heated area (m)

Greek symbols

μ dynamic viscosity (kg/(m·s))

ρ fluid density (kg/m^3)

σ standard deviation

θ phase angle (°)

Subscripts

b bulk

e inlet of the heated section

in inlet of the test section

j section number

k circumferential position number

l lower position

o outlet of the test section

s outlet of the heated section

Email address: dcrespi@umh.es (D. Crespí-Llorens)

u upper position

wi inner wall

amb ambient

L losses

<u>Dimensionless groups</u>

Re_n net Reynolds number, $\rho U_n D/\mu$

Re_{osc} oscillatory Reynolds number, $\rho(2\pi f x_0)D/\mu$

Ψ velocity ratio, Re_{osc}/Re_n

Pr Prandtl number, $\mu c_p/k$

Nu Nusselt number, hD/k

1. Introduction

Heat transfer enhancement has attracted a significant degree of attention in the previous decades and still new techniques are being researched and developed. Traditionally, enhancement techniques have been classified [4] as active or passive, depending if they require or not an external power source, respectively. Nowadays, combined techniques are gaining relevance [8, 1, 3], finding remarkable potential applications. This is the case of the Oscillatory Baffled Reactors (OBR) and their use for reactions with a high residence time. A conventional continuous tubular reactor made of smooth tubes would require high Reynolds numbers to operate under turbulent flow conditions, which are needed to achieve good radial mixing. However, a high Reynolds number implies (for a given fluid and geometry) a high velocity and, consequently, an extremely long tube in order to fulfil the high residence time. An additional drawback would be the excessive pressure drop and pumping power. As a solution, a set of equally-space baffles (passive technique) are introduced in the tube and an oscillatory flow (active technique) is superimposed on a low net flow. This combination leads to a flow mechanism characterized by cyclic vortex dispersion upstream and downstream of the baffles. As a result, an augmentation of heat and mass transfer is achieved.

Flow patterns are one of the most studied aspects in OBRs. The aim is to identify the radial mixing mechanism and the influence of the operating conditions on the onset of the flow asymmetry and the chaotic behaviour. The first noteworthy study dates from 1989, when Brunold et al. [5] tested several baffle spacings: $l = 1 - 2D$. They observed that the flow oscillation generates vortices downstream of the baffles during both oscillation half cycles, causing an intense mixing. The authors identified the optimal baffle spacing at $l = 1.5D$, a value which is currently a reference for the OBRs design.

Mackay et al. [12] performed the first study focused on the instability in OBRs. By using a qualitative flow visualization technique, the authors collected in a map the flow behaviour (asymmetric or not) as a function of the oscillatory Reynolds number, Re_{osc}, and the Strouhal number, St. For the range of Strouhal numbers tested ($0.3 < St < 2$), the flow was asymmetric at an oscillatory Reynolds number of order 200.

Zheng et al. [22] developed a three-dimensional numerical model, validated with PIV results. The model is used to obtain a two-dimensional map which shows the level of flow symmetry as a function of the Strouhal number and the oscillatory Reynolds number, i.e., pure oscillatory flow conditions. The authors observed that the maximum oscillatory Reynolds number at which the flow becomes asymmetric is 225, at a Strouhal number of 1.0. Below a Strouhal number of 0.5, there is a reduction of the critical oscillatory Reynolds number. At a Strouhal number of 0.1 the asymmetry can be seen at an oscillatory Reynolds number of 100. It is finally highlighted that, in spite of not being a clear correlation, there is a connection between the flow asymmetry and the mixing intensity.

Another aspect which has been a focus of attention since the OBRs conception is heat transfer. It has been motivated by the need of a right sizing of thermal circuits for heat addition or removal when endothermic or exothermic reactions take place in the OBR, or when the temperature is a key factor for the reaction.

Mackley et al. [14] studied heat transfer in a tube with equally-spaced one-orifice baffles. The range of dimensionless numbers tested was a Prandtl number of 124, a net Reynolds number, Re_n, between 100 and 700 and an oscillatory Reynolds number of 200-1600 (for a given net Reynolds number). The main conclusions were: 1) under steady flow conditions the baffles imply a significant heat transfer augmentation in comparison to a smooth tube, 2) under compound flow conditions (net and oscillatory flow) the effect of the oscillation on heat transfer was limited in the absence of baffles, while there was a significant increase for the baffled tube. Mackley and Stonestreet [13] extended the previous study, carrying out two experimental campaigns: the first one focused on the study of the oscillating amplitude, and the second one on the superposition of the net and the oscillatory flow. Regarding the amplitude, the effect on the Nusselt number was found to be moderate, with a slight increase for lower oscillating amplitudes (and the same maximum oscillatory flow velocity). The authors confirmed that an increase on the Re_n or the Re_{osc} imply a higher heat transfer rate. They found that at high net Reynolds numbers, i.e., when the velocity ratio Re_{osc}/Re_n is reduced, all the results converged to the steady flow results ($Re_{osc} = 0$). The research group P4G [18], from Cambridge University, studied the heat transfer in OBRs obtaining similar conclusions.

Law et al. [11] studied a similar OBR under cooling conditions and constant wall temperature. The tested ranges were: $Re_n = 200 - 1400$, $Re_{osc} = 0 - 2700$ and

$Pr = 4.5 - 9$. The authors found that, for all the net Reynolds numbers tested, at high values of the oscillatory Reynolds number the Nusselt number converged to a given value. According to the authors, this observation could be related to the minimum axial dispersion observed by Smith and Mackley [19] in the range of oscillatory Reynolds numbers 800-1000. Above that range the radial mixing and the perturbation of the boundary layer would not rise.

From the previous review, we can conclude that, while the OBRs have been widely studied, there are some relevant aspects of their performance that have not been properly addressed. That is the case of the flow patterns study in conditions with net and oscillatory flow, which is the common operating condition for the OBRs, or the study of the relation between flow asymmetry and mixing intensity.

Regarding the heat transfer studies pointed out in this introduction, the minimum net Reynolds number tested is of the order of 200, a value which has been identified as the critical net Reynolds number for baffle inserts in recent studies [16]. Therefore, it would be interesting to extend the tested ranges to conditions where the net flow would be laminar and, consequently, there would exist a poor heat transfer under steady flow conditions.

This work presents a rigorous experimental study of a one-orifice baffled tube, using a set of experimental techniques which complement each other: hydrogen visualization and PIV. Besides, a thermohydraulic test rig has been used to characterise the heat transfer under uniform heat flux conditions. The study is focused on several points related to the heat transfer process and the interaction between the oscillatory and net flows at low net Reynolds numbers.

2. Experimental method

This section describes the facilities and experimental methods which have been used for this work. Three experimental methodologies have been employed: hydrogen bubbles flow visualization, particle image velocimetry, and heat transfer measurements. For that, two experimental facilities have been built: a visualization facility and a thermohydraulic testing facility.

The geometry under study, depicted in Fig. 1, consists of a tube with an inner diameter $D = 32$ mm and annular equally spaced insert baffles made of PEEK plastic, being their separation distance of $1.5D$ and the inner baffle diameter of $0.5D$. From now on, the space between consecutive baffles will be referred to as *cell tank*.

Different mixtures of water and propylene glycol are used as working fluid. Viscosity of the different fluid preparations has been measured to determine the exact ratio of water and glycol. The rest of the fluid thermophysical properties are deduced out of this ratio [2].

The experimental uncertainties derived from the here described methodology are summarised in Table 1.

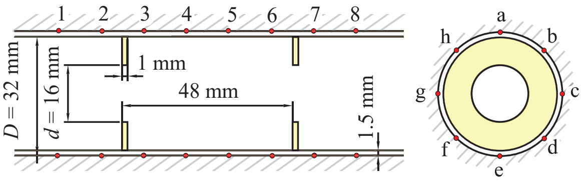

Figure 1: Baffle geometry and thermocouple arrangement in the test section.

	Average	Maximum
Re_n	3.4%	4.9%
Re_o	4.2%	5.2%
x_0/D	2.0%	2.8%
Pr	3.3%	4.0%
Nu	7.1%	11.5%

Table 1: Uncertainties of results.

2.1. Visualization facility

The facility depicted in Fig. 2a is used to perform visualization experiments under different working conditions. The working fluid is prepared in a reservoir tank (10), which is connected to a closed loop circuit. By the use of a chiller (8) connected through a plate heat exchanger (7) and an electric heater (11), the working fluid temperature is controlled. On the one hand, the system is built to generate a net flow through the test section (4) by using a centrifugal pump (1). On the other hand, a hydraulic cylinder (14) is able to produce a 0.12 Hz to 1.2 Hz sinusoidal oscillatory flow in the test section (4). Both systems can be engaged at the same time, producing a compound flow: net and oscillatory. A flow control valve (2), has been used to ensure a stable net flow. The position of the hydraulic cylinder (14) is measured by a magnetostrictive position sensor (15). The visualization section (4) is surrounded by an acrylic box, which is filled with the working fluid and avoids image aberration.

In this facility, two visualization experimental techniques have been used: hydrogen bubbles and Particle Image Velocimetry (PIV), which are described in detail in the following sections. Flow field images for both type of experiments are captured by a 1280×1024 pix^2 CMOS MotionScope M3 high speed camera.

2.2. Hydrogen bubble visualization

The configuration used to perform hydrogen bubbles experiments is depicted in Fig. 2b. A copper wire is inserted along the cross section diameter of the test tube, so that the symmetry plane containing the wire and the tube axis will be seeded with bubbles. For that, salt is dissolved in the fluid ($\approx$ 2 g/dm^3), and a voltage difference is produced between the formerly mentioned copper wire and a metallic accessory of the pipe loop, downstream the test section. By controlling the DC voltage difference, the velocity of bubbles generation is

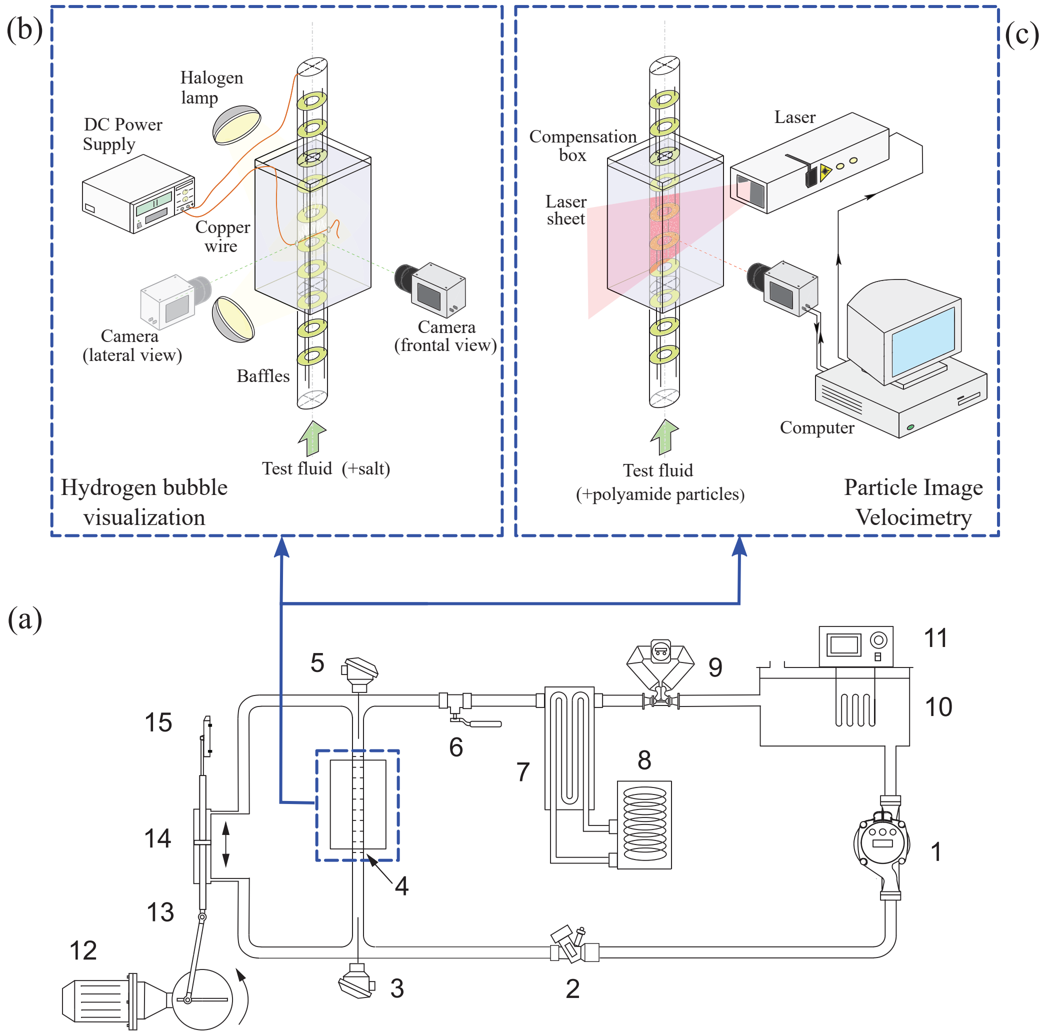

Figure 2: (a) Visualization facility, (b) image acquisition setup for hydrogen bubbles experiments and (c) PIV experiments. Visualization facility parts: (1) centrifugal pump, (2) flow control valve, (3) P100 inlet, (4) baffles, (5) PT100 outlet, (6) manual valve, (7) plate heat exchanger, (8) chiller, (9) Coriolis flowmeter, (10) reservoir tank, (11) electric heater, (12) gear-motor assembly, (13) connecting rod-crank, (14) hydraulic cylinder, (15) magnetostrictive position sensor.

adjusted. Illumination to the flow is provided by two 55 W halogen lamps. Fig. 2b shows two possible positions of the camera. One shows a *frontal view* of the seeded plane, and provides most of the information of the flow field. The other shows a *lateral view* of the seeded plane, and allows us to detect significant velocities in transverse direction to the symmetry plane.

2.3. Particle Image Velocimetry

The configuration used to perform PIV experiments is depicted in Fig. 2c. To this aim, the flow is seeded with 57 μm polyamide particles with a density of 1051 kg/m^3. The symmetry plane is then illuminated by a 1 mm thick laser light sheet of 808 nm wavelength. By taking two consecutive images of the seeded flow with the Motionscope M3 camera, and knowing the time elapsed between shots, the flow velocity pattern can be obtained by the PIV algorithm.

PIV is carried out by using the PIVlab code, version 2.31, for Matlab [21]. After PIV image pre-processing (histogram equalization, intensity highpass and intensity capping), 97.7% of the velocity vectors are found valid, $PPR > 2$ (peak-to-peak ratio). Image processing is carried out by the adaptive FFT (Fast Fourier Transform) cross correlation algorithm in four steps, where the last interrogation area size is 24×24 pix^2. Post-processing includes the application of a global filter and two self-developed local filters, which are based on the signal-to-noise ratio and on repeatability of the results across image pairs representing equivalent flow fields.

2.3.1. Determination of the initial phase. Instantaneous flow rate calculation

The initiation of the images acquisition is triggered by a photoelectric sensor. Nevertheless, deviations from the exact position or delays in the photoelectric sensor signal can lead to a wrong estimation of the cycle beginning (initial phase). In order to improve the determination of the initial phase, a PIV based instantaneous flow rate estimation is used.

The instantaneous flow rate has been obtained as a derived measurement, using the flow axial velocity along the radial direction of the tube. To that aim, the OBR test section is divided in a center circle and a series of annular spaces with the same width, given by the PIV algorithm interrogation area (IA) size. Each annular space, i, has a width $d_i = D/(2\ n_d)$, where n_d is the number of IA in the radial direction. Thus, the axial velocity, u_i, is known for several radial positions, r_i, from $r = 0$ to $r = D/2$. r_i is given by the position of the IA center. The flow rate is then estimated by numerical integration,

$$\dot{V} = \sum_{i=1}^{n_d} u_i A_i = \frac{\pi}{4} \sum_{i=1}^{n_d} u_i \left[\left(r_i + \frac{d_i}{2} \right)^2 - \left(r_i - \frac{d_i}{2} \right)^2 \right] \quad (1)$$

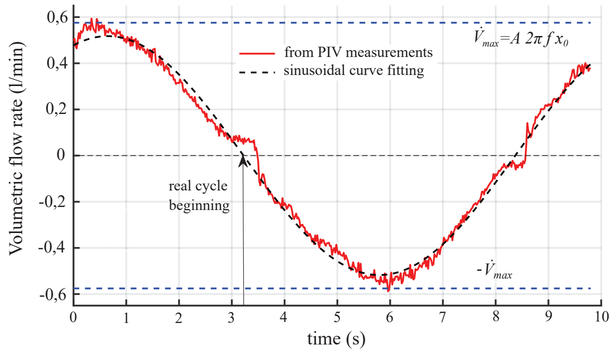

Figure 3: Instantaneous volumetric flow rated obtained from the PIV velocity field.

Fig. 3 shows the volumetric flow rate evolution throughout an oscillation cycle for a test with pure oscillatory flow. As can be observed, the waveform is mainly sinusoidal and the highest deviations are obtained around the null mean velocity point, when the highest PIV inaccuracies are expected. In addition, the maximum and minimum theoretical flow rates, derived from the measured oscillation amplitude and frequency, are plotted as well in the figure. The maximum experimental values are close to the theoretical values, within a range of a 10%.

The previous methodology is only valid when the flow is axisymmetric, i.e., the axial velocity at each radial position can be considered as representative of the associated annular space. For the asymmetric case, the phase-averaged instantaneous flow rate has been used.

However, the flow rate curve obtained with this method has a significant noise level. Thus, if the raw signal were used to calculate the cycle beginning the results would be inaccurate. Instead, raw data are fitted to a sinusoidal curve. The zero crossing of this curve is considered as a better approximation for the cycle beginning. In Fig. 3 the sinusoidal fitting and the estimation of the cycle beginning are presented as well.

2.4. Heat transfer facility and methodology

A specific facility has been built for heat transfer tests (Fig 4). The main loop contains a reservoir tank (1), a Coriolis flowmeter (3) and a gear pump assembly (2) consisting in three pumps in parallel. The pumping system circulates the working fluid through a 32 mm diameter AISI 316 stainless steel tube (5), where the test section is located. Equally spaced insert baffles are arranged through the test section. Input and output temperatures are measured by two PT100 temperature probes (4, 7). A uniform heat flux is provided to the fluid by Joule effect, using a transformer and an autotransformer (10) connected to the steel tube upstream and downstream of the test section. The separation distance between electrodes is $L_h = 26D$ mm. A secondary loop, which has been described in a previous work [16], is in charge of fluid temperature control. The whole fa-

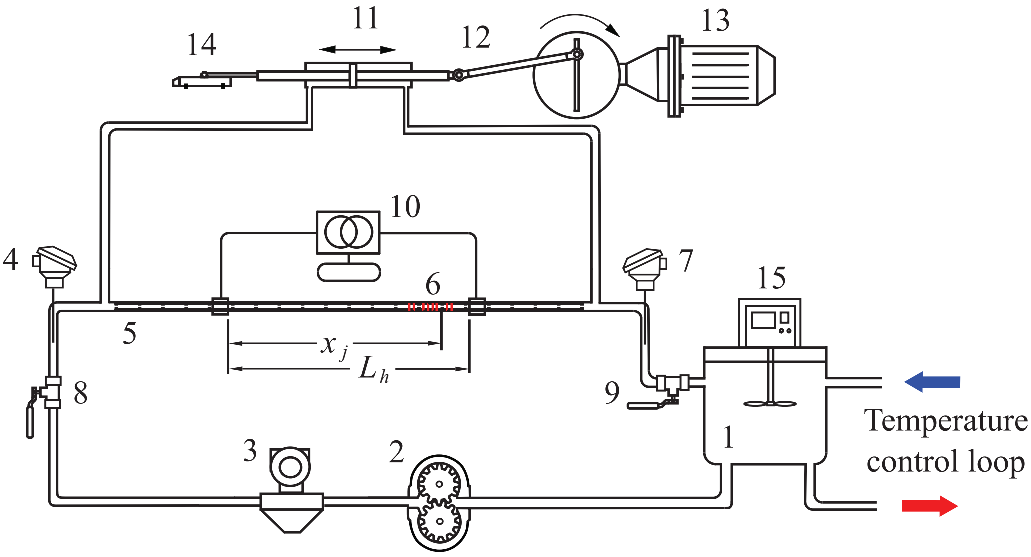

Figure 4: Heat transfer facility setup. (1) Main Tank, (2) positive displacement pumping system, (3) Coriolis flowmeter, (4) input flow temperature probe B 1/10 DIN PT100, (5) insert baffles, (6) type T thermocouples set, (7) output flow temperature probe, (8 and 9) manually operated valves, (10) autotransformer, (11) double effect hydraulic piston, (12) connecting rod-crank, (13) gear-motor assembly, (14) magnetostrictive position sensor, (15) agitator.

cility and specially the test section are properly insulated.

As in the visualization facility, the sinusoidal oscillatory flow in the test section is generated by a rod-crank mechanism (12, 13) attached to a double effect piston (11), which is connected in parallel to the test section. A magnetostrictive sensor (14) is used to determine the position of the piston. The assembly is capable of creating an oscillatory flow with a frequency ranging from 0.47 to 4.7 Hz.

In order to measure the tube wall temperature, a total of 8×8 type T thermocouples are attached to the steel tube outer diameter at 8 axial positions, each containing 8 thermocouples equally spaced around the tube cross section (see Fig. 1). As can be observed in Fig. 5, the 8 test sections are located well downstream of the first electrode ($x_1 = 20D$), in order to ensure periodicity of the flow.

Fig. 5 is an schematic representation of the variables involved in the local and average Nusselt numbers calculation. The bulk fluid temperature can be estimated from the measurement of inlet fluid temperatures ($T_{b,i}$) the heat provided (Q) by the autotransformer and the estimation of heat losses ($Q_{L,e}$, Q_L, $Q_{L,s}$). Then, the local Nusselt number at each testing cross section can be obtained as

$$Nu_j = \frac{q''}{T_{wi,j} - T_{b,j}} \cdot \frac{D}{k_j} \tag{2}$$

where q'' is the heat flux provided to the fluid, $T_{b,j}$ is the estimated bulk temperature of the fluid at this section, $T_{wi,j}$ is the mean inner wall tube temperature and k_j is the thermal conductivity of the fluid. The inner wall temperature is calculated using a one-dimensional conduction model [10]. Finally, the Nusselt number Nu is obtained as the average of local Nusselt numbers $Nu = \sum Nu_j$.

3. Results

This section presents the experimental results and the analysis of the flow characteristics for the pure oscillatory flow and for the compound flow.

The dynamic nature of the oscillatory flow makes it impractical to collect and/or present its full complexity throughout the entire oscillation cycle. Consequently, the results shown in this work for PIV measurements correspond to 8 equally spaced phases of the oscillation cycle, as shown in Fig. 6 (blue line). However, for a pure oscillatory flow and due to its temporal symmetry, the significant positions are reduced to 4. Besides, results for hydrogen bubbles experiments are presented for significant cycle positions, but those with a higher image quality have been selected for their presentation in the figures.

3.1. Oscillatory flow

Two types of visualization experiments have been carried out to analyse the flow behavior inside the device in conditions of pure oscillatory flow (nonexistent net flow). On the one hand, hydrogen bubbles experiments provide a qualitative evaluation of the flow conditions and a general overview of the full oscillation cycle. On the other hand, PIV experiments provide quantitative results of the flow pattern within the device for the most significant positions of the oscillation cycle. For this flow, the oscillatory Reynolds number is used, Re_{osc}.

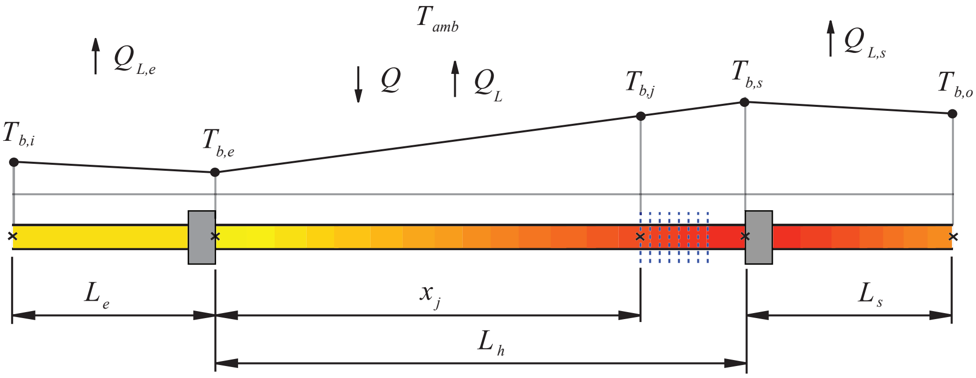

Figure 5: Temperature variation along the test section.

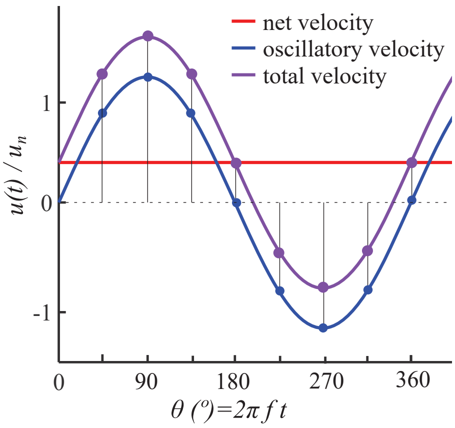

Figure 6: Phases of the oscillation cycle for flow field representation (PIV technique).

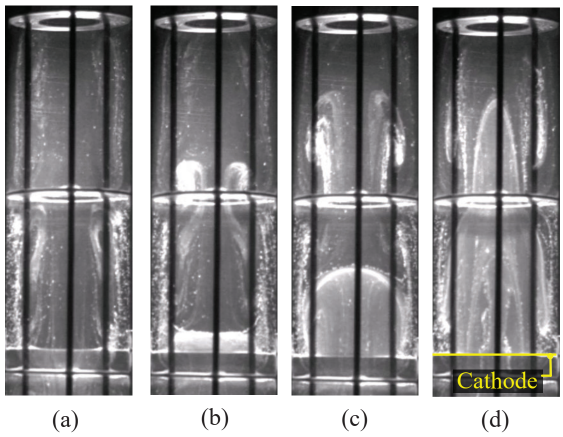

Figure 7: Front view of the hydrogen bubble seeded plane for Re_{osc} = 32. (a) $\theta = -22°$, (b) $\theta = 22°$, (c) $\theta = 55°$ y (d) $\theta = 90°$. $x_0/D = 0.5$.

3.1.1. Qualitative observation of the full cycle

Hydrogen bubbles experiments have been carried out for oscillatory Reynolds numbers ranging in $Re_{osc} \in [32, 160]$ and an oscillation amplitude of $x_o/D = 0.5$.

Fig. 7 presents the visualization results for Re_{osc} = 32. Pictures show two consecutive cell tanks, being the copper wire (cathode) located at bottom of the lower tank. Fig. 7a shows the flow field just before the change of direction in the oscillation cycle. At this point, the downwards oscillation half cycle is about to finish and its recirculations can be observed. They are located in the peripheral fluid region, all along the cell tank. At Fig. 7b the flow field slightly after the new cycle beginning is shown. A contraction of the flow is observed upstream of the baffle, while downstream of it, a core jet with associated peripheral recirculations begins to develop. The structure has evolved in Fig. 7c to a mushroom shape, where the center jet and recirculations cover a longer fraction of the cell tank. Finally at Fig. 7d the jet and the outer recirculations cover the full span of the cell tank, after which the flow will decelerate and the same structure will be repeated in the opposite direction.

The front view of the flow field for Re_{osc} = 150 does

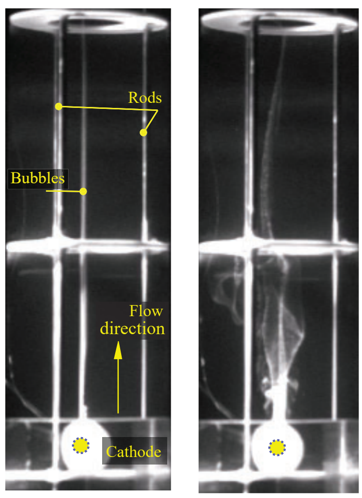

Figure 8: Lateral view of the hydrogen bubble seeded plane for instant $\theta = 180°$, for (a) Re_{osc} = 32 y (b) Re_{osc} = 150. $x_0/D = 0.5$.

not provide clear information about the influence of the oscillatory Reynolds number in this range, as significant deviations from the formerly commented case cannot be clearly identified. In order to observe further differences when varying the oscillatory Reynolds number, the same experiments are carried out for a different position of the camera. In this case, the flow plane which has been seeded with hydrogen bubbles is observed from a lateral position (see *Lateral view* in Fig. 2b). From this perspective, the seeded plane in the two-dimensional image captured by the camera is observed as a straight line. Fig. 8 shows this view of the flow for $Re_{osc} = 32$ and $Re_{osc} = 150$. As can be seen, no velocity is detected in perpendicular direction to the seeded symmetry plane for $Re_{osc} = 32$. This allow us to conclude that the flow is axisymmetric, showing laminar characteristics all throughout the oscillation cycle. However, the behaviour is different for $Re_{osc} = 150$, where velocities in perpendicular direction to the plane are significant and they fluctuate across cycles, showing a much more complex and unstable nature of the flow.

[Front and lateral views of the flow for both oscillatory Reynolds numbers are presented in Video 1 for the full oscillation cycle.] [Video 1 - Caption: Front and lateral views of the pure oscillatory flow for $Re_{osc} = 32$ and $Re_{osc} = 150$.]

The observed flow structure within the analysed range of oscillatory Reynolds numbers presents in any case significant momentum transfer in radial direction. This has two benefits for the use of this device as an OBR: flow mixing and heat transfer enhancement. However this qualitative technique does not allow us to quantify such benefits, other than that they seem to increase with the oscillatory Reynolds number. This point is addressed in the following sections.

3.1.2. Flow pattern

By using PIV, measurements and observations of the flow field have been carried out for oscillatory Reynolds numbers within the range $Re_{osc} \in [30, 175]$ for $x_o/D = 0.5$.

In this section, velocity fields obtained with PIV (Figures 9, 10) are depicted in non-dimensional form v^+, by dividing the local velocity by the maximum velocity of the field:

$$v^+ = \frac{v(r,x)}{\max(v(r,x))} \tag{3}$$

This velocity v^+ is only used for flow field representation purposes.

However, this non-dimensional form hides the differences in the bulk velocity between different cycle positions. To provide such information, velocity profiles are presented with a different non-dimensional velocity v^*.

$$v^* = \frac{v(r,x)}{2\pi f x_0} \tag{4}$$

where $2\pi f x_o$ is the maximum bulk velocity of the cycle, which occurs for the middle position of the piston $\theta = 90°,\ 270°$.

Firstly, the general characteristics of the flow are analysed as a function of the oscillatory Reynolds number. The results show two different flow regions which will be analysed.

On the one hand, in Section 3.1.1 the flow has been found to have laminar characteristics and to be axisymmetric for low Reynolds numbers. On the other hand, PIV results show that the flow pattern is periodic for the same range of Re_{osc}. This is observed in the flow patterns plotted in Fig. 9a and 9b at position $\theta = 180°$ for $Re_{osc} = 51$. The figures present, respectively, the phase-average flow field and the instantaneous flow field at the same position of the cycle, showing no significant differences between them.

The results for $Re_{osc} > 130$ show a completely different behaviour. Fig. 9c and 9d show, respectively, the average and instantaneous flow fields at position $\theta = 180°$ of the cycle for $Re_{osc} = 175$. As can be seen, there is no temporal periodicity across cycles and the instantaneous flow field (Fig. 9d) is asymmetric, showing recirculations which are not present in the phase-average field (Fig. 9c). This chaotic behaviour is also confirmed by the observations with hydrogen bubbles in Section 3.1.1.

Secondly, the flow field throughout the oscillation cycle is studied for the flow regimes which have been identified. Fig. 10a shows the most significant cycle positions $\theta = 0°,\ 45°,\ 90°,\ 135°$ for $Re_{osc} = 51$. These flow patterns agree with the observation using hydrogen bubbles, but PIV results provide resolution and quantification of the different effects. For example, for positions $\theta = 0°,\ 90°,\ 135°$, the size of the center jet (about $0.5D$) and the recirculations are observed. Besides, the representation for $\theta = 45°$ shows the flow pattern after the oscillation cycle has started. At this point a jet is developing downstream of the baffles, but the flow pattern in the cell tank is dominated by low velocities in the core region of the flow and high velocities in the peripheral region, most probably due to inertial forces. This structure disappears for $\theta = 90°$, where velocities in the outer region have changed their direction due to the effect of the central jet.

Fig. 11a presents the velocity profile at the middle cross section of the cell tank for 8 phase positions of the oscillation cycle. It can be observed that for $\theta = 0°$ the core flow is still in negative direction, becomes slightly positive for $\theta = 45°$ and increases with θ up to more than four times the maximum bulk velocity for $\theta = 90°$. Besides it presents a symmetrical behaviour for $180° < \theta < 360°$.

As an example of the experiments for higher oscillatory Reynolds numbers, Fig. 11b presents the equivalent results for $Re_{osc} = 175$. They show a similar average behaviour of the flow to the case with a lower Re_{osc}: flow field dominated by the alternative creation of a jet in the

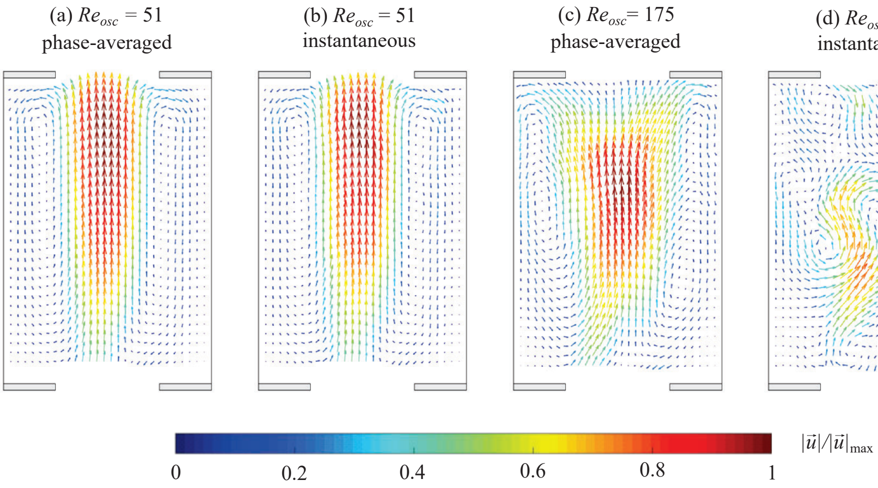

Figure 9: Phase-average vs. instantaneous velocity fields. Pure oscillatory flow

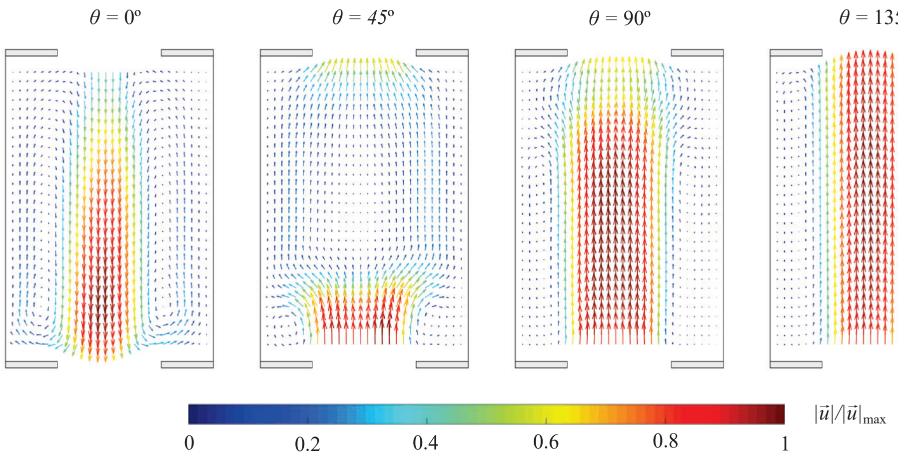

(a) Re_{osc} = 51.

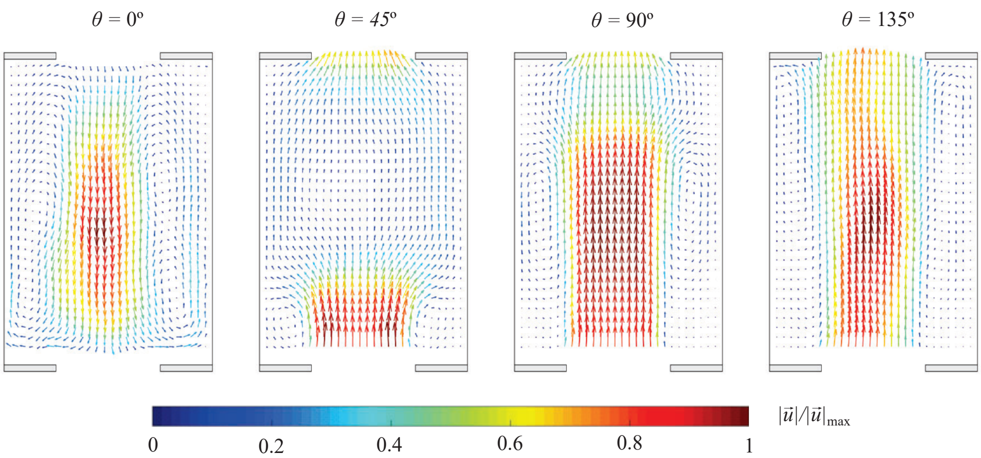

(b) Re_{osc} = 175.

Figure 10: Phase-average velocity field for different instants of the oscillation cycle. Pure oscillatory flow.

core flow region and recirculations on the outer flow region. Apart from the different nature of the flow, which is not time periodic nor axisymmetric, the flow velocity is also different. As shown in Fig. 11a, the velocities for $Re_{osc} = 175$ are in general higher than for $Re_{osc} = 51$, presenting maximum velocities of 6 times the maximum average velocity of the cycle, again for $\theta = 90°$.

3.2. *Compound flow*

The object of study in this section is the compound flow inside the baffled tube, meaning that an oscillatory flow is superimposed on a net flow. To that aim, the standard Reynolds number for flow in tubes is used. To avoid misunderstanding, from here on it will be referred to as the net flow Reynolds number, Re_n.

Besides, the ratio between the Reynolds numbers of the oscillatory flow and the net flow (velocity ratio) is used as well,

$$\Psi = \frac{Re_{osc}}{Re_n} = \frac{2\pi f x_0}{U_n} \tag{5}$$

The flow behaviour in this section is analysed by flow pattern visualization (Section 3.2.1) and heat transfer measurements (Section 3.2.2).

3.2.1. *Flow pattern*

The analysis of the superimposed net and oscillatory flows requires the evaluation of the velocity ratio, Ψ. To that aim, experiments have been carried out for $Re_n = 34$ while varying the oscillatory flow in the range $1.5 < \Psi < 5$.

Fig. 12a shows the phase-averaged velocity fields at 8 phase positions for a periodic flow $Re_{osc} = 51$ and $\Psi = 1.5$. In comparison with the flow pattern observed for a pure oscillatory flow (Fig. 10 a)), the flow is very similar, but presents no temporal symmetry between the positive and negative oscillation half cycles. As can be observed, the compound flow runs in the direction of the net flow (forwards) longer than in the opposite direction (backwards). Consequently, the central flow jet covers the full cell space during a significant portion of the oscillation cycle $\theta = 90°, 135°, 180°$ in forward direction, while the recirculation vortices observed in backward direction $\theta = 315°$ do not move along the full cell space. This would most probably result in unsatisfactory mixing in radial direction during this part of the cycle.

Fig. 12b shows, for the same net flow Reynolds number, the phase average velocity fields for a higher oscillatory Reynolds number $Re_{osc} = 175$ and $\Psi = 3.5$. As can be observed, the similarity of the flow pattern to the one of the pure oscillatory flow is higher, for higher values of Ψ. For this case, the effect of the net flow is still evident, and the forwards flow lasts longer that the backwards one. However, flow mixing during the backwards flow is much higher than for $\Psi = 1.5$.

In addition, the effect of the Reynolds numbers in the compound flow maintaining the same velocity ratio (Ψ) has been studied. For that, experiments for

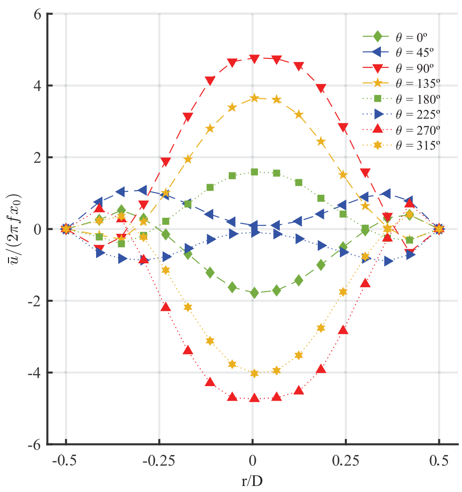

(a) $Re_{osc} = 51$.

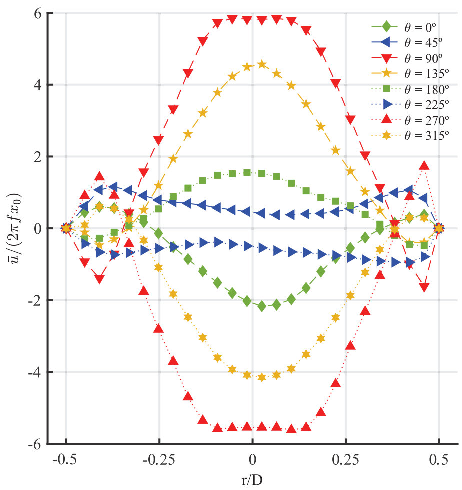

(b) $Re_{osc} = 175$.

Figure 11: Phase-average velocity profiles at the middle cross section of a cell tank for different instants of the oscillation cycle. Pure oscillatory flow.

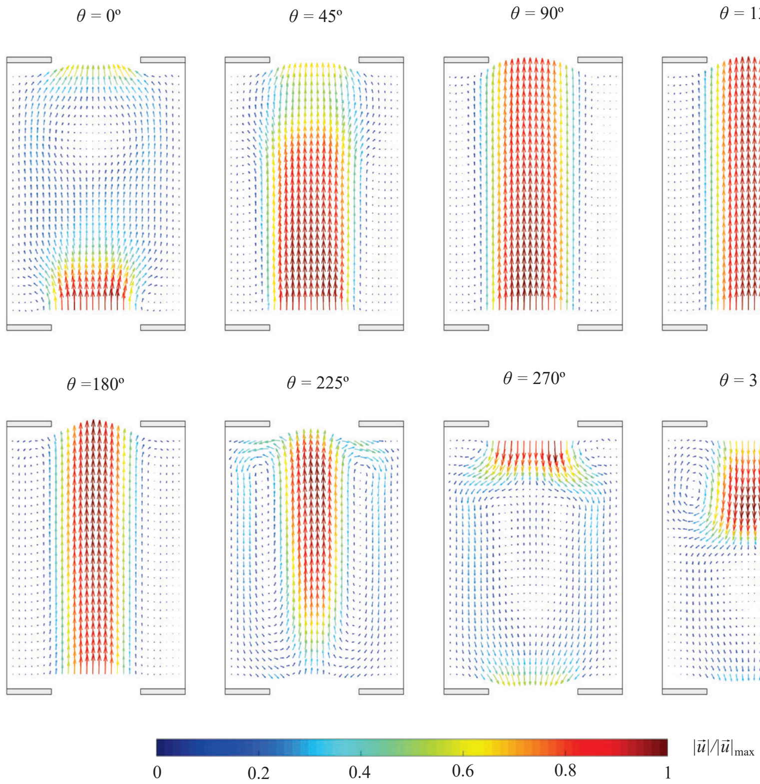

(a) $\Psi = 1.5$ ($Re_{osc} = 51$)

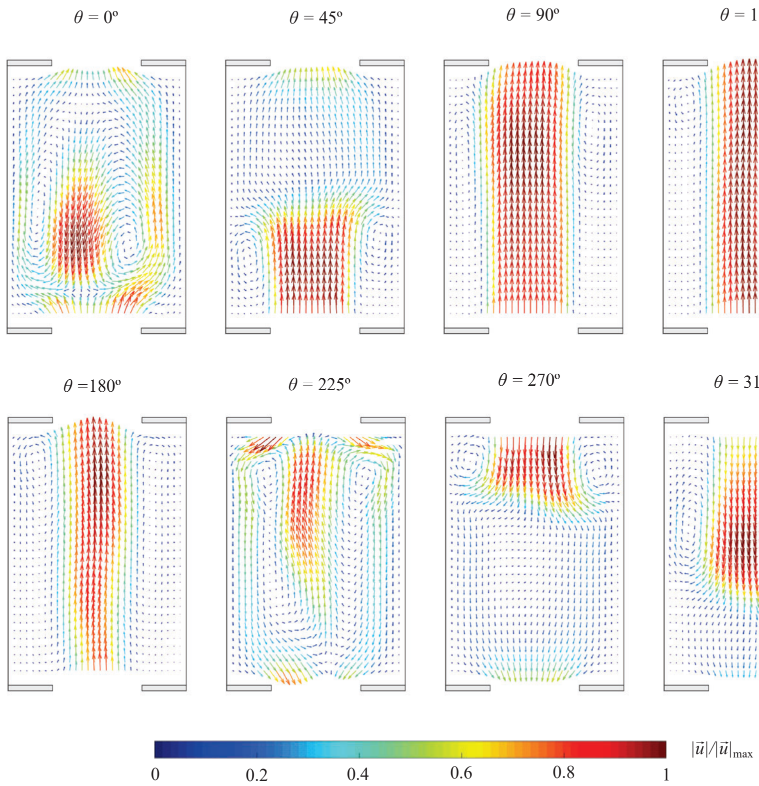

(b) $\Psi = 3.7$ ($Re_{osc} = 175$)

Figure 12: Phase-average velocity field of a compound flow for $Re_n = 34$. Net flow direction: upwards.

$\Psi = 1.7$ have been carried out while simultaneously varying both Reynolds numbers $Re_{osc} \in [51, 90]$ and $Re_n \in [28, 54]$. Results for the phase position $\theta = 225°$ are shown in Fig. 13. As can be observed, the flow field is time-periodic for the case with $Re_{osc} = 51$, while the periodicity is lost for the experiment with $Re_{osc} = 90$ and the flow becomes unstable, which will increase mass transfer in radial direction.

Finally, the mixing intensity of the flow is analysed through the use of axial-radial velocity ratio proposed by Manninen et al. [15],

$$\overline{R}_v = \left[\sum_{i=1}^{n_s} \frac{1}{R_v(t_i)} \right]^{-1} \quad (6)$$

where n_s is the number of image pairs acquired during an oscillatory cycle and R_v is defined as

$$R_v(t_i) = \sum_{j=1}^{n_w} \frac{|u_j(t_i)| \cdot r_j}{|v_j(t_i)| \cdot r_j} \quad (7)$$

where r_j is the distance from the interrogation area (IA) center to the pipe axis and n_w is the number of IAs for which the corresponding velocity vector has been calculated.

A value of $\overline{R}_v < 3.5$ has been found to guarantee a good mixing [7].

Fig. 14a presents the axial-radial velocity ratio $\overline{R}_v$ for two values of the net Reynolds number. For both cases, when the flow velocity ratio is low, $\Psi = 1$, the axial-radial velocity ratio is far over 3.5, indicating a poor mixing. Nonetheless, as the oscillation becomes more important (increasing Ψ), flow mixing increases significantly. Thus, a proper mixing ($\overline{R}_v < 3.5$) is achieved for the experiments with $Re_n = 27$ at $\Psi = 4.5$ and for $Re_n = 55$ at $\Psi \approx 2$. It can be then concluded that increasing the flow velocity ratio and/or increasing both Reynolds numbers, enhances mass transfer in radial direction.

The same results of the axial-radial velocity ratio $\overline{R}_v$, together with the results of a pure oscillatory flow, are plotted in Fig. 14b in order to observe the isolated effect of the oscillatory Reynolds number. The main conclusion which can be extracted is that a proper mixing in radial direction is obtained for oscillatory Reynolds numbers above 130. Thus, as pointed out by Stonestreet and Van Der Veeken [20], the axial mixing is not only function of the flow velocity ratio Ψ, but also of the Reynolds numbers. The results of this study show that only with both an oscillatory Reynolds number $Re_{osc} > 130$ and a flow velocity ratio $\Psi > 2$ a proper mixing level can be guaranteed.

3.2.2. Heat transfer

All heat transfer tests have been performed for the same Prandtl number, $Pr = 150$, and oscillation amplitude, $x_o/D = 0.5$. For each net Reynolds number tested, the Grashof number is kept constant and the oscillatory Reynolds number was modified. The three net Reynolds numbers tested are in the laminar flow regime, $Re_n < 170$, according to previous studies [16].

Local Nusselt number. The visualization results for the pure oscillatory flow and the compound flow have shown that the flow patterns change with time (throughout the oscillation cycle) and space (along the cell tank). Previous results have studied the local Nusselt number variation in baffle geometries under steady flow conditions [9], showing a strong dependence on the net Reynolds number.

The thermocouples arrangement allows us to obtain the local Nusselt number, based on the averaged wall temperature at each of the eight measuring cross-sections. In Figure 15 the local Nusselt number is plotted as a function of the dimensionless axial distance (measured as the number of diameters from the position of the baffle previous to the measuring sections), for $Re_n = 65$ and a total number of four different oscillatory Reynolds numbers. The relative position of the baffles is indicated by vertical dashed lines.

The solution for the steady case ($Re_{osc} = 0$) is presented in Fig. 15a. As can be noticed, the distribution has an inverted U-shaped pattern: downstream of the baffles, the local Nusselt number increases progressively until it reaches a maximum. This region is associated with a separation and reattachment flow structure [16]. Once the flow is fully adhered to the wall, the boundary layer thickness increases in the axial flow direction, which yields a progressive reduction of the Nusselt number.

Another aspect to highlight is that the local Nusselt number variation along the cell tank decreases with Re_{osc} for $Re_{osc} > 102$.In order to further quantify this trend, a parameter which measures the mean local Nusselt number variation in comparison to the mean Nusselt number along the cell tank is calculated. This parameter, NV_s, is obtained as:

$$NV_s = \frac{\sum_{j=1}^{8} |Nu_j - Nu_m|}{8\, Nu_m} \quad (8)$$

and can be considered as a measurement of the uniformity of the Nusselt number distribution.

The parameter is plotted in Fig. 16 as a function of the oscillatory Reynolds number for the three net Reynolds numbers tested. The three cases show the same trend, from a value corresponding to the steady case there is an increase on the Nusselt number variation, reaching the maximum at $Re_{osc} = 100 - 130$. Above this critical value the variation decreases asymptotically to a value of 5-10% at $Re_{osc} > 400$.

Unexpectedly, for low values of Re_{osc} the oscillatory flow superposition leads to an increase of the local Nusselt number variation. This can also be observed in Fig. 15b, $Re_{osc} = 102$: the laminar flow oscillation implies a significant increase of the local Nusselt number at the cell tank center, while the shadow effect caused by the baffles is augmented.

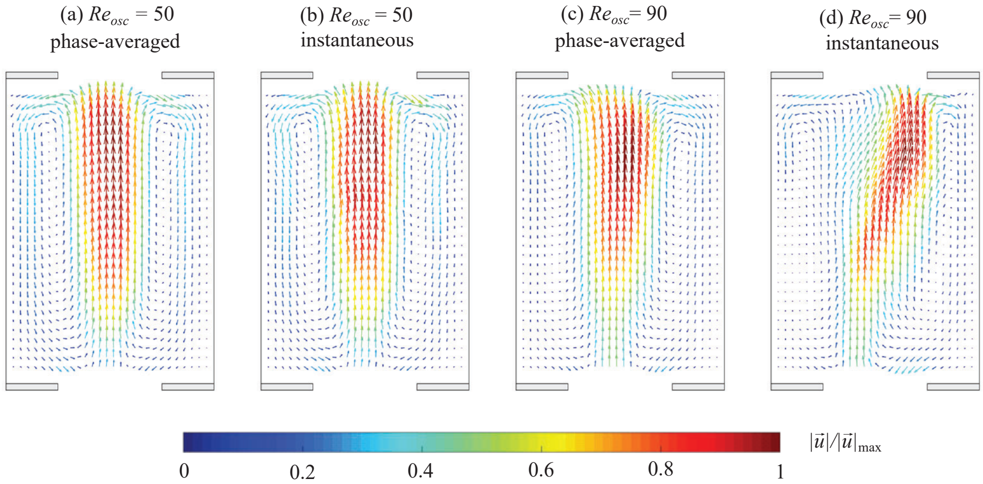

Figure 13: Velocity field of a compound flow with Ψ = 1.7 and θ = 225° for Re_{osc} = 50 (left) and Re_{osc} = 90 (right).

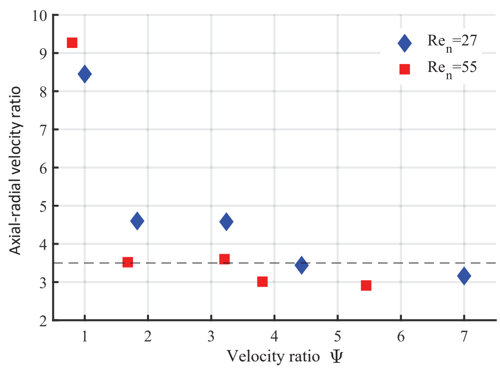

(a)

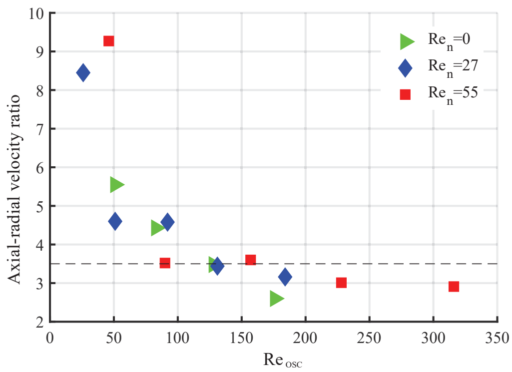

(b)

Figure 14: Axial-radial velocity ratio as a function of (a) the flow velocity ratio Ψ and (b) the oscillatory Reynolds number Re_{osc} .

Above an oscillatory Reynolds number $Re_{osc} > 130$, the flow becomes chaotic [12] by the effect of the oscillatory flow. The intense mixing during both oscillation half cycles causes a more uniform local Nusselt number along the cell tank.

Thermal stratification. The experimental arrangement also makes possible the study of the potential existence of mixed convection. The parameter used to quantify the effect of the buoyancy is the difference between the upper and lower inner wall temperatures, averaged for the eight measuring sections.

The average temperature difference is plotted in Fig. 17 as a function of the oscillatory Reynolds number. As it can be observed, for the three steady cases (Re_{osc} = 0) the stratification effect is evident, with differences of around 20-30 °C between the upper and lower wall temperature. The test for each net Reynolds number has been performed with a different heat flux and, consequently, a different Grashof number, so no conclusions shall be obtained about the effect of the net Reynolds number on the stratification.

When the oscillatory flow is superimposed there is a clear progressive reduction of the temperature difference, which has been already observed in tri-orifice baffled tubes at low Reynolds numbers [17]. The temperature difference is null at an oscillatory Reynolds number of $Re_{osc} \approx 130-150$ for the three net Reynolds numbers tested. This limit value is very similar to the critical oscillatory Reynolds number at which the oscillatory flow becomes chaotic. Thus, the chaotic flow is enough to cancel mixed convection for the range of Grashof numbers tested.

Average Nusselt number. While the local Nusselt number provides information related to the flow behaviour, the most important variable for a proper design is the mean average Nusselt number. In Fig. 18 the average Nusselt number is shown as a function of the oscillatory Reynolds number.

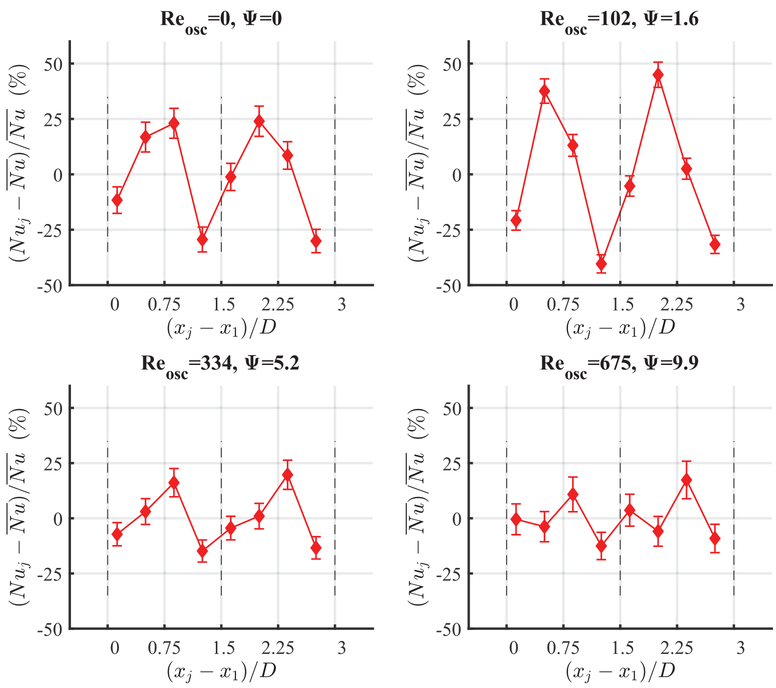

Figure 15: Local Nusselt number vs dimensionless axial distance for Re_n = 65, Pr = 150. (a) Re_{osc} = 0, (b) Re_{osc} = 102, (c) Re_{osc} = 334, (d) Re_{osc} = 675.

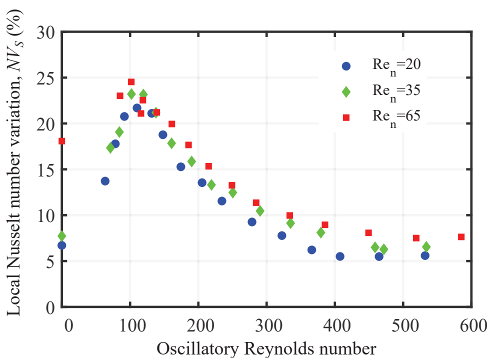

Figure 16: Local Nusselt number variation as a function of the oscillatory Reynolds number.

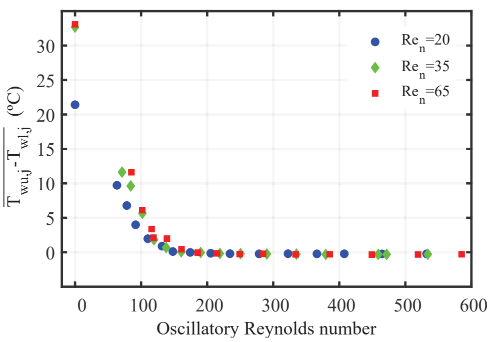

Figure 17: Mean difference between the upper and lower thermocouples as a function of the oscillatory Reynolds number.

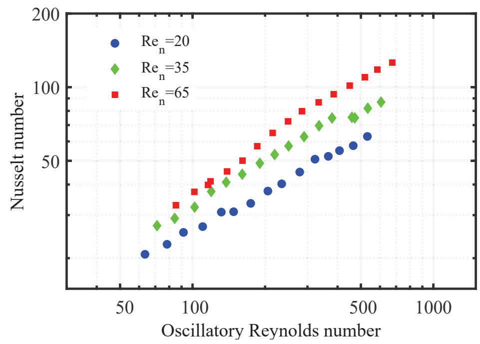

Figure 18: Averaged Nusselt number as a function of the oscillatory Reynolds number.

There are two main trends in the results, one is the increase in the Nusselt number when the net Reynolds number increases, and the other is the augmentation of the Nusselt number when the oscillatory Reynolds number is increased. Both trends have already been observed in baffled tubes with oscillatory flow [13, 11, 18].

For the range of velocity ratios tested, $\Psi \leq 20$, no noticeable saturation has been observed, as the slope of the Nusselt number seems to be the same for the tested range of oscillatory Reynolds numbers.

Wall temperature standard deviation. The outside wall temperature standard deviation has been used previously to distinguish the different flow regimes in smooth tubes under steady flow conditions [6]. There are 64 thermocouples along the measuring section and the mean value of the standard deviations for each thermocouple is used as the relevant parameter. In this way, we aim at quantifying the local wall temperature variation throughout time and not between different positions (in the axial or azimuthal direction).

However, it is reasonable to think that for a lower temperature difference between the wall and the bulk fluid, the standard deviation of the wall temperature would also be lower for the same flow pattern. This observation is relevant because the tests have been done keeping the Grashof number approximately constant (same heat flux), and a higher oscillatory Reynolds number implies a higher convection coefficient, and, consequently, a reduction of the wall-bulk fluid temperature. In order to compensate this effect, a dimensionless standard deviation of the difference between the wall and the bulk fluid is considered:

$$\frac{\overline{\sigma(T_{wi,jk} - T_{b,j})}}{\bar{T}_{wi} - \bar{T}_{b,j}} \cdot 100 \tag{9}$$

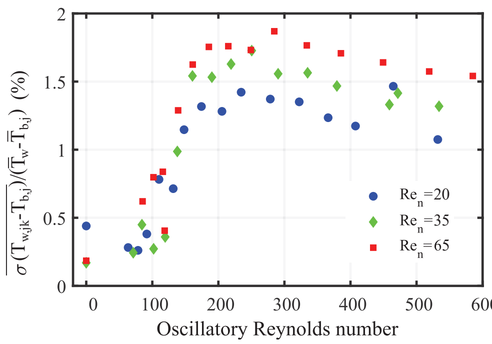

Figure 19: Dimensionless wall temperature standard deviation as a function of the oscillatory Reynolds number.

This dimensionless standard deviation is shown in Fig. 19. For the three net Reynolds numbers tested the values are quite low, 0.5%, for the steady flow case and for oscillatory flow Reynolds numbers $Re_{osc} < 100$. This non-zero but low values can be again justified by the repeatability of the thermocouples. Above Re_{osc} = 100 there is a sharp increase in the dimensionless standard deviation up to a 1.5 % (three times the value found in the laminar flow regime) at $Re_{osc} = 200$. This range coincides again with the critical Reynolds number at which the flow is chaotic, confirming that the flow behaviour has a remarkable effect on the wall temperature, caused by the deviation of the central, colder stream, which moves towards the walls and increases the wall temperature variation.

In the higher range of oscillatory Reynolds numbers tested ($Re_{osc} = 200 - 600$) this value does not suffer significant changes, suggesting a flow with a similar level of chaos, or, at least, at the level at which the chaos can have an influence on the wall temperature variation over time.

4. Conclusions

- Under oscillatory flow conditions, flow axisymmetry and temporal periodicity have been observed for $Re_{osc} < 130$, pointing out a two-dimensional laminar flow behaviour. During the negative and positive half cycles, recirculations are created downstream of the baffles and they grow along the cell length. Above $Re_{osc} \approx 130$, the flow becomes asymmetric and three-dimensional.
- The effect of increasing the velocity ratio (Ψ) or the oscillatory Reynolds number is to increase the mixing intensity (reducing the axial-radial velocity ratio, $\overline{R_v}$). To achieve an appropriate mixing ($\overline{R_v} < 3.5$), a high enough oscillatory Reynolds number, $Re_{osc} \geq 130$, is required, in addition to a high velocity ratio ($\Psi \geq 2$).
- Both net and oscillatory Reynolds numbers have a positive impact on the Nusselt number. In the range tested, up to 3-5 times increases on the heat transfer rate have been measured in comparison to the steady flow case. No saturation of the heat transfer rate has been detected for the range of velocity ratios tested ($\Psi < 20$).
- The results have shown a close connection between the local Nusselt number (along a cell tank) and the flow structure, with a more uniform Nusselt number distribution when the oscillatory flow becomes chaotic, $Re_{osc} \approx 130$.
- The existence of mixed convection has been observed under laminar steady flow conditions and with a superimposed oscillatory for $Re_{osc} < 150$. The onset of the chaotic oscillatory flow removes the thermal stratification of the flow.
- The onset of the chaotic flow regime has a significant effect on the standard deviation of the wall temperature throughout time. There is a sharp increase of this value in the range $100 < Re_{osc} < 200$.

Acknowledgments

The authors gratefully acknowledge the financial support of the project DPI2015-66493-P by Ministerio de Economía y Competitividad (MINECO, Spain) and the European Regional Development Fund (ERDF).

References

[1] Amiri, S., Taher, R., Mongeau, L., 2017. Quantitative visualization of temperature field and measurement of local heat transfer coefficient over heat exchanger elements in sinusoidal oscillating flow. Experimental Thermal and Fluid Science 85, 22 – 36. doi:https://doi.org/10.1016/j.expthermflusci.2017.02.008.

[2] ASHRAE, 2001. ASHRAE fundamentals handbook.

[3] Özer Bağcı, Dukhan, N., 2018. Impact of pore density on oscillating liquid flow in metal foam. Experimental Thermal and Fluid Science 97, 246 – 253. doi:https://doi.org/10.1016/j.expthermflusci.2018.04.020.

[4] Bejan, A., Kraus, A.D., 2003. Heat transfer handbook.

[5] Brunold, C.R., Hunns, J.C.B., Mackley, M.R., Thompson, J.W., 1989. Experimental observations on flow patterns and energy losses for oscillatory flow in ducts containing sharp edges. Chemical Engineering Science 44, 1227–1244. doi:https://doi.org/10.1016/0009-2509(89)87022-8.

[6] Everts, M., Meyer, J., 2018. Heat transfer of developing and fully developed flow in smooth horizontal tubes in the transitional flow regime. International Journal of Heat and Mass Transfer 117, 1331–1351.

[7] Fitch, A.W., Jian, H., Ni, X., 2005. An investigation of the effect of viscosity on mixing in an oscillatory baffled column using digital particle image velocimetry and computational fluid dynamics simulation. Chemical Engineering Journal 112, 197–210. doi:10.1016/j.cej.2005.07.013.

[8] Kamsanam, W., Mao, X., Jaworski, A.J., 2015. Development of experimental techniques for measurement of heat transfer rates in heat exchangers in oscillatory flows. Experimental Thermal and Fluid Science 62, 202 – 215. doi:https://doi.org/10.1016/j.expthermflusci.2014.12.008.

[9] Kiml, R., Magda, A., Mochizuki, S., Murata, A., 2004. Rib-induced secondary flow effects on local circumferential heat transfer distribution inside a circular rib-roughened tube. International Journal of Heat and Mass Transfer 47, 1403–1412. doi:10.1016/j.ijheatmasstransfer.2003.09.026.

[10] Kutz, M., 2006. Heat Transfer Calculations.

[11] Law, R., Ahmed, S., Tang, N., Phan, A., Harvey, A., 2018. Development of a more robust correlation for predicting heat transfer performance in oscillatory baffled reactors. Chemical Engineering and Processing: Process Intensification 125, 133–138.

[12] Mackay, M., Mackley, M., Y., W., 1991. Oscillatory flow within tubes containing wall or central baffles. Trans IChemE 69, 506–513.

[13] Mackley, M.R., Stonestreet, P., 1995. Heat transfer and associated energy dissipation for oscillatory flow in baffled tubes. Chemical Engineering 50, 2211–2224.

[14] Mackley, M.R., Tweddle, G.M., Wyatt, I.D., 1990. Experimental heat transfer measurements for pulsatile flow in baffled tubes. Chemical Engineering Science 45, 1237–1242. doi:10.1016/0009-2509(90)87116-A.

[15] Manninen, M., Gorshkova, E., Immonen, K., Ni, X.W., 2013. Evaluation of axial dispersion and mixing performance in oscillatory baffled reactors using CFD. Journal of Chemical Technology & Biotechnology 88, 553–562. doi:10.1002/jctb.3979.

[16] Muñoz-Cámara, J., Crespí-Llorens, D., Solano, J., Vicente, P., 2020a. Experimental analysis of flow pattern and heat transfer in circular-orifice baffled tubes. International Journal of Heat and Mass Transfer 147, 118914. doi:10.1016/j.ijheatmasstransfer.2019.118914.

[17] Muñoz-Cámara, J., Solano, J., Pérez-García, J., 2020b. Experimental correlations for oscillatory-flow friction and heat transfer in circular tubes with tri-orifice baffles. International Journal of Thermal Sciences 156, 106480. doi:10.1016/j.ijthermalsci.2020.106480.

[18] Paste Particle and Polymer Processing group (P4G), . https://www.ceb.cam.ac.uk/research/groups/rg-p4g/archive-folder/pfg/ofm-folder/ofm-advantages-enhancement-of-heat-transfer-rates.

[19] Smith, K., Mackley, M., 2006. An experimental investigation into the scale-up of oscillatory flow mixing in baffled tubes. Chemical Engineering Research and Design 84, 1001–1011.

[20] Stonestreet, P., Van Der Veeken, P.M., 1999. The effects of oscillatory flow and bulk flow components on residence time distribution in baffled tube reactors. Chemical Engineering Research and Design 77, 671–684. doi:10.1205/026387699526809.

[21] Thielicke, W., Stamhuis, E.J., 2014. PIVlab – Towards User-friendly, Affordable and Accurate Digital Particle Image Velocimetry in MATLAB. Journal of Open Research Software 2, 1–10. doi:10.5334/jors.bl.

[22] Zheng, M., Li, J., Mackley, M.R., Tao, J., 2007. The development of asymmetry for oscillatory flow within a tube containing sharp edge periodic baffles. Physics of Fluids 19, 1–15. doi:10.1063/1.2799553.